Retrieval of atmospheric properties and surface bidirectional reflectances over land from POLDER/ADEOS

Marc A Leroy, J. Deuzé, F.M. Bréon, O. Hautecoeur, M. Herman, J. Buriez, D. Tanré, S. Bouffiès, P. Chazette, Jean-Louis Roujean

JOURNAL OF GEOPHYSICAL RESEARCH, VOL. 102, NO. D14, PAGES 17,023–17,037, JULY 27, 1997

Retrieval of atmospheric properties and surface bidirectional reflectances over land from POLDER/ADEOS

M. Leroy,[1] J. L. Deuzé,[2] F. M. Bréon,[3] O. Hautecoeur,[1] M. Herman,[2] J. C. Buriez,[2] D. Tanré,[2] S. Bouffiès,[3] P. Chazette,[3] and J. L. Roujean[4]

Abstract. Polarization and Directionality of the Earth's Reflectances (POLDER) is a new instrument devoted to the global observation of the polarization and directionality of solar radiation reflected by the Earth-atmosphere system. It will fly onboard the ADEOS platform in 1996. This paper outlines the improvements expected from POLDER in the description of atmospheric aerosols and water vapor over land, and of surface bidirectional reflectances. It then gives a detailed description of the operational algorithms which are implemented in the "land surface and atmosphere over land" processing line. This line is part of an effort initiated by Centre National d'Etudes Spatiales (the French Space Agency) to develop lines of products in order to facilitate the exploration of POLDER's new capabilities by the international science community. Emphasis is given in this paper to the presentation of the principles, physical rationale, and elements of validation of the algorithms of this processing line. The main products are (1) for each orbit segment, the amount and type of aerosols, the water vapor content, and bidirectional reflectances corrected for atmospheric effects, and (2) every 10 days, global maps of surface directional signatures, of hemispherical surface reflectances, and of parameters describing the statistical distribution of aerosol and water vapor content. These products will be made available to all interested investigators. The most innovative algorithms of the processing line are (1) cloud detection, based on a series of tests involving reflectance thresholds, oxygen pressure estimates, and analysis of polarized radiance in the rainbow direction, (2) retrieval of aerosol optical thickness and type from directional polarized radiance measurements, and (3) retrieval of surface directional signature through an adjustment of a time series of directional reflectance measurements with a semiempirical bidirectional reflectance model.

1. Introduction

Before the end of the century, a series of Earth-orbiting satellites will carry several advanced, well-calibrated instruments designed to provide global observations of the Earth's oceans, land, and atmosphere. Among them, Polarization and Directionality of the Earth's Reflectances (POLDER) is a new instrument devoted to the global observation of solar radiation reflected by the Earth surface-atmosphere system. Two identical versions of this instrument will fly on the Japanese Advanced Earth Observing Satellite (ADEOS) platforms scheduled for launch in 1996 and 1999. In order to facilitate the exploration of POLDER new capabilities by the international science community, Centre National d'Etudes Spatiales (CNES) has initiated an effort aiming at the development of processing lines of science products. Three lines are developed (1) land surfaces and atmosphere over land, (2) ocean color and aerosols over ocean, and (3) Earth radiation budget, water vapor, and clouds. The products will be processed operationally in the Toulouse center of CNES and made available to all interested scientific investigators. The "land surface and atmosphere over land" processing line, which is the subject of this paper, is designed to support the science objectives related to the monitoring of land surfaces, as well as atmospheric aerosols and water vapor over land.

Aerosols have a large effect on the Earth radiation budget both directly, by modifying the Earth's albedo, and indirectly, by playing an important role in the formation of condensation nuclei which trigger cloud formation [*Charlson et al.*, 1992]. Also, aerosols over land may affect vegetation growth [*Swap et al.*, 1992]. The cycling of the aerosols, that is, aerosol sources, transport in the atmosphere, and sinks, is of interest in various fields of science, e.g., desertification, pollution, and biogeochemical cycles. A quantitative assessment of the aerosol effects on the Earth's climate and environment and, in particular, that of anthropogenic aerosols requires a global mapping of the type and concentration of tropospheric aerosols.

Atmospheric water vapor is a key climatologic variable because of its capacity to drive energy exchanges between the ocean and atmosphere and within the atmosphere by releasing latent heat. Moreover, of all atmospheric gases, water vapor exhibits the largest spatial and temporal variations and has the potential to drive a large positive feedback in global warming scenarios [*Rind et al.*, 1991]. Accurate global mapping of at-

[1]Centre d'Etudes Spatiales de la Biosphère, Unité Mixte Centre National d'Etudes Spatiales/Centre National de la Recherche Scientifique/Université Paul Sabatier, Toulouse, France.
[2]Laboratoire d'Optique Atmosphérique, USTL-Centre National de la Recherche Scientifique, Villeneuve d'Ascq, France.
[3]Laboratoire de Modélisation du Climat et de l'Environnement, Commissariat à l'Energie Atomique/Saclay, Gif-sur-Yvette, France.
[4]Centre National de Recherches en Météorologie, Météo-France, Toulouse, France.

Paper number 96JD02662.
0148-0227/97/96JD-02662$09.00

Table 1. Characteristics of POLDER Channels

Central Wavelength, nm	Bandwidth, nm	Polarization	Dynamic Range	Main Mission
443	20	no	0.05–0.22	Ocean color
443	20	yes	0.05–1.1	Vegetation, aerosols, Earth radiation budget
490	20	no	0.034–0.17	Ocean color
565	20	no	0.019–0.11	Ocean color
670	20	yes	0.013–1.1	Vegetation, aerosols, Earth radiation budget
763	10	no	0.007–1.1	Cloud top pressure
765	40	no	0.007–1.1	Vegetation, aerosols, cloud top pressure
865	40	yes	0.007–1.1	Vegetation, aerosols, Earth radiation budget
910	20	no	0.007–1.1	Water vapor amount

The dynamic range is expressed in reflectances for the Sun at zenith.

mospheric water vapor is an important objective of the Global Energy and Water Cycle Experiment (GEWEX) program.

The monitoring of land surfaces is another major science objective, stressed by the International Geosphere-Biosphere Program (IGBP). It is necessary to identify precisely the major biomes on the surface of the planet and to be able to detect changes in their composition or mapping, due either to anthropogenic or climatic causes. Deforestation and desertification are among the most critical and timely issues of land cover change. Land monitoring from space is also a key methodological step to understanding and modeling the general functioning of the terrestrial biosphere system, i.e., vegetation growth, maturity, and decay, at regional or global scales [*Fung et al.*, 1987; *Ruimy et al.*, 1994]. Finally, land surfaces are a major component of the climate system. Land monitoring can provide valuable information on the boundary conditions that should be specified in general circulation models (GCM) to describe accurately the exchanges of mass, momentum, and energy at the biosphere-atmosphere interface [*Dickinson*, 1984; *Sellers et al.*, 1994].

The POLDER data should provide a valuable contribution to these different issues. The scientific processing applied operationally to the data is a key issue to meeting this scientific challenge. The goal of this paper is to present the principles of the "land surface and atmosphere over land" processing line, the physical rationale of its algorithms, and the elements of validation of these algorithms when available. Sections 2 and 3 of the paper summarize the main characteristics of the POLDER instrument concept and outline the potential contributions of the POLDER products in the field of atmospheric properties over land, and land surface monitoring. Section 4 then presents a general overview and a detailed description of the algorithms and products of the processing line. Note that the framework and goals of this processing line have some similarities with those of the lines of products related to the atmosphere [*King et al.*, 1992] and to the surface [*Running et al.*, 1994] developed together with the moderate-resolution imaging spectroradiometer (MODIS) instrument.

2. Instrument Characteristics

The POLDER instrument is described extensively by *Deschamps et al.* [1994]. The description is briefly summarized here. POLDER is composed of a bidimensional CCD matrix, a rotating wheel that carries filters and polarizers, and a wide (114°) field of view lens. The field of view seen by the CCD matrix is ±43° along track and ±51° across track. The pixel size on the ground at nadir is 6×7 km^2 for the ADEOS altitude of 800 km. The rotating wheel carries filters which allow spectral measurements at eight different wavelengths. The spectral bands are described in Table 1. One image of each spectral band is acquired every 19.6 s. The bands at 490 and 565 nm are used with a low dynamic range (see Table 1) and are thus unused over land surfaces where they will saturate frequently. There is a large overlap between successive images. A surface target is viewed up to 14 times during the satellite overpass with various viewing angles. Thus the POLDER instrument concept allows sampling of the bidirectional reflectance distribution function (BRDF). The directional configuration changes each day owing to orbital shift on successive days. Thus, after a few days, assuming cloud-free conditions, the successive orbits provide a complete description of the BRDF, in the limits of the instrument field of view.

Three of the channels (443, 670, and 865 nm) also measure the linear polarization of the incident light. This is achieved by three measurements with polarizers turned by steps of 60°. A combination of the three measurements yields the Stokes parameters I, Q, U, from which the total radiance $L = I$, the polarized radiance $L_{pol} = (Q^2 + U^2)^{1/2}$, and the direction of polarization may be deduced. Radiative transfer simulations and experimental evidence show that the polarization is mostly linear for natural targets (the fourth Stokes parameter V is very small compared to the other three), so that the triplet (I, Q, U) is sufficient to describe the polarization of reflected sunlight.

The expected radiometric resolution, in terms of noise equivalent differential reflectance (NeDR) at the top of the atmosphere, is better than 5×10^{-4} (with the Sun at zenith) for the bands used for land surface monitoring. The objectives of multiangular, multispectral, multitemporal, and absolute radiometric calibration accuracies are 1%, 1%, 2%, and 2–3%, respectively, for these bands [*Deschamps et al.*, 1994]. As for the geometry, the multipolarization, multispectral, multiangular, and multitemporal geometric registrations should be better than 0.1, 0.1, 0.2, and 0.3 pixel, respectively. These performances are needed for accurate derivation of the polarized radiance, polarization direction, BRDF, and vegetation spectral indices.

3. Contributions of POLDER

3.1. Tropospheric Aerosols Over Land

Global monitoring of tropospheric aerosols remains a challenge. The major difficulty is that the aerosol contribution to

the top of the atmosphere (TOA) reflectance is generally much smaller than the surface contribution. Different possibilities of aerosol monitoring exist, however. For example, *Kaufman and Sendra* [1988] have shown that the aerosol contribution to the reflectance can be determined when the surface reflectance is low, which is the case over dark, dense vegetation in the blue (443 nm) and in the red (665 nm). However, the usual vegetation indices may be inadequate for the selection of dense vegetation pixels because of the perturbation of these indices by aerosol scattering. A possibility is to base the selection on observations at longer wavelengths (2.1 or 3.7 μm) that are much less affected by aerosol scattering (except for dust) and are still sensitive to the surface characteristics [*Kaufman and Tanré*, 1996]. Algorithms assuming that the surface is invariant have been also used for multitemporal studies. If the surface reflectance is stable, the temporal evolution of the satellite signal is related to the temporal evolution of the aerosol content [*Fraser et al.*, 1984; *Kaufman et al.*, 1990]. The retrieval of the aerosol optical thickness may be achieved also from the contrast degradation [*Tanré et al.*, 1988; *Holben et al.*, 1992] over ground targets exhibiting both a high temporal stability and a large spatial heterogeneity, such as some desert areas. Aerosol events may also be detected over desert areas by using infrared imagery [*Legrand et al.*, 1988, 1989], since the radiative temperature of the atmosphere-surface system is affected by the presence of a dust aerosol layer.

These methods, although powerful over specific areas, cannot be used for global analysis without crude interpolation schemes. Moreover, a shortcoming of the methods that use a single directional reflectance measurement to derive aerosol parameters is that the observation is only sensitive to the product of the aerosol phase function and the aerosol optical thickness. Thus an assumption is needed on the aerosol phase function if the optical thickness is to be estimated.

The information provided by POLDER will permit the development of a new approach to retrieving the aerosol loading at a global scale and providing some indication of aerosol type [*Herman et al.*, this issue]. The principle of this approach is that the main contribution to the TOA polarized radiance at short wavelengths is due to the aerosols and molecules of the atmosphere, while the contribution of the surface is generally smaller and less variable than that of the aerosols. The contribution of atmospheric molecules, although significant at short wavelengths, is nearly invariant and can be easily modeled. That of the surface is more variable, but experimental evidence shows that it can be modeled with some confidence at least for dense vegetation cover [*Rondeaux and Herman*, 1991] or for bare soils [*Bréon et al.*, 1995]. Thus the aerosol contribution to the polarized radiance can, in principle, be extracted from the measurement. For typical aerosol optical thickness, this contribution is approximately proportional to the product of the aerosol optical thickness τ_a and of the aerosol polarized phase function, which depends on the observation geometry primarily through the scattering angle Θ. Thanks to the bidirectional capabilities of POLDER, retrievals of this product in different directions are possible. The magnitude of the aerosol contribution is related to the aerosol optical thickness, while the detailed shape of the angular variations of the polarized radiance is related to the aerosol polarized phase function. The latter should, in turn, permit the discrimination of various types of aerosols, characterized by their refractive index and size distributions.

Global mapping of aerosol content and type will be useful in several respects. The impact of atmospheric aerosols on the Earth's radiative budget has been demonstrated. They directly perturb the radiative budget by their scattering and absorption of sunlight [*Coakley and Cess*, 1985]; they modify the cloud microphysics by acting as cloud condensation nuclei, and as a result, they also impact cloud radiative properties [*Twomey et al.*, 1984]. As POLDER observes the same pixel under different viewing angles and in several spectral channels, the anisotropy of the reflected radiation field is directly measured. Thus the determination of the reflected solar flux from satellite will be more accurate, and a better assessment of the impact of aerosols on the radiative budget is expected. In-cloud processes modify the aerosol size distribution, as shown by *Hoppel et al.* [1990], with an increase of aerosol size due to a coagulation process. POLDER gives a good opportunity to study this feedback by connecting the cloud albedo to the concentration and size distribution of aerosols surrounding the clouds. *Kaufman and Nakajima* [1993] performed such a study using advanced very high resolution radiometer (AVHRR) data with smoke particles emitted by biomass burning in the Amazon Basin.

Aerosol particles also make an important contribution to many biogeochemical cycles. Estimation of dust deposition, for instance, should be possible with POLDER, since the main uncertainty comes from the aerosol size distribution [*Fraser*, 1976; *Dulac et al.*, 1992].

3.2. Precipitable Water Vapor Over Land

Thanks to the SSM/I data (microwave measurements by the special sensor microwave imager onboard the U.S. Defense Meteorological Satellites Program platforms), precipitable water is reliably retrieved over the oceans, where the surface microwave emissivity is well known. This method cannot be applied over land because of the land emissivity variability. Over land, infrared sounders like Tiros N operational vertical sounder (TOVS) are able to retrieve the water vapor profile from the atmospheric temperature profile. However, the resulting accuracy may be very poor in regions where most of the water vapor is concentrated in the lower atmospheric layers, like in Sahelian regions [*Holben et al.*, 1990; *Justice et al.*, 1991]. Precipitable water vapor can also be derived from conventional radiosoundings by vertically integrating pressure and relative humidity profiles, but radiosoundings are, unfortunately, sparse and unevenly distributed over the globe.

POLDER provides a new opportunity to retrieve the total atmospheric water vapor amount on a daily basis with a comparatively high spatial resolution (20 km). The method uses a differential absorption technique [*Frouin et al.*, 1990; *Gao and Goetz*, 1990; *Kaufman and Gao*, 1992] that exploits measurements collected by the 910-nm channel centered on a water vapor absorption band. The radiances measured at this wavelength are compared to those measured at 865 nm, where the water vapor absorption is very weak. The ratio of these two radiances is related to the atmospheric water vapor amount. Although some uncertainties in this approach result from aerosol scattering and surface reflectance variations between the two wavelengths, global accuracies of the order of 10% are expected [*Bouffiès et al.*, 1995] (see section 4.5 below).

The water vapor products of POLDER will not be available in real time, and therefore an assessment of the potential impact of these products on weather forecasting in a fully operational context is not possible at present. On the other hand, the validation of water vapor retrieval over land from

POLDER using sunphotometer network will permit an evaluation of the validity of the differential absorption technique. It will then be interesting to determine experimentally whether the real-time availability of POLDER data could improve short-term weather forecasts. In the long term, this may promote the use of a similar instrument for operational weather forecasting.

3.3. Bidirectional Surface Reflectances

Towards accurate, frequent measurements of surface reflectance. Monitoring of terrestrial vegetation from satellites at global or regional scales requires accurate and frequent measurements of surface reflectance. The key improvement brought by POLDER in this context will be to provide, at high temporal repetitiveness, measurements of surface reflectance corrected for atmospheric effects and brought to the same directional standard.

Directional effects are a major source of perturbations for land surface monitoring. They are intrinsically related to the desired high repetitiveness of observations. A given pixel is seen under very different view angles in successive observations from a polar orbiting satellite, or under different Sun angles from a geostationary platform. Temporal variations of the measurements of AVHRR resulting from changes in the observation geometry have a strong amplitude, typically 50–100% of the average signal [*Gutman*, 1987; *Roujean et al.*, 1992a].

The atmosphere is another major source of perturbations in land surface sensing. While the part of the signal due to atmospheric molecule scattering can be predicted with sufficient accuracy, the variations of absorbing gases and aerosols at fine temporal and spatial scales can induce severe fluctuations of the signal measured by the sensor. Choosing appropriate spectral bands permits either the obtention of a signal insensitive to absorbing gases, or the retrieval of some information on these gases that allows a correction of their influence on the observed signal (see section 3.2). The part of the signal due to aerosols is generally much more difficult to correct (see section 3.1). For example, the uncertainties in the correction of aerosol effect are of the same order of magnitude as the surface reflectance for vegetated areas in the visible [e.g., *Tanré et al.*, 1992; *Kaufman and Tanré*, 1996].

Thus the processing of AVHRR observations requires the composition of a time series of measurements to simultaneously minimize atmospheric and directional effects, and also the effects of poor cloud detection. A data-compositing method widely applied to AVHRR data is the maximum value composite (MVC) technique [*Tarpley et al.*, 1984]. Its principle is to select, during a given period of composition, from 1 week to 1 month, the AVHRR data which maximize the normalized differential vegetation index (NDVI). The MVC technique has been a standard routine in the context of vegetation monitoring [e.g., *Tucker et al.*, 1985; *Justice et al.*, 1985]. More recent developments are based either on improvements of the MVC technique, using more sophisticated data filtering [*Viovy et al.*, 1992], or on correction of directional effects derived from the original data set [*Gutman*, 1991; *Leroy and Roujean*, 1994; *Wu et al.*, 1995; *Ba et al.*, 1995].

The accuracy of this latter method should be much higher with POLDER, which will cover directional space much better than AVHRR, in particular, in azimuth [*Deschamps et al.*, 1994]. Consequently, the minimum time period of measurements needed to derive by compositing a measure normalized for directional effects is expected to be shorter with POLDER than with AVHRR.

The improvement of atmospheric corrections (with a better account of aerosols; see section 3.1) and access to highly repetitive measurements of surface reflectance corrected for directional effects with POLDER are expected to improve, at regional and global scales, both land cover studies and net primary production estimates. Classifications of land cover types at continental scales which classify coarse resolution pixels on the basis of the NDVI temporal signature [*Townshend et al.*, 1987] should take advantage of an improvement of the accuracy of observed surface reflectances. Terrestrial net primary production may be derived from an evaluation of the absorption of photosynthetically active Sun radiation, in turn related to the NDVI [*Prince*, 1991; *Ruimy et al.*, 1994; *Field et al.*, 1995]. The limitations of this approach result from the crude description of the functional link between production and sensor measurements, but also from perturbating effects in satellite measurements [*Maisongrande et al.*, 1995].

Directional signature. Another important aspect is that, after compositing of satellite measurements, the land surface BRDF will be available at regional and global scales. Several science products can take advantage of this new signature.

Albedo: The BRDF measurements will permit an estimate of spectral hemispherical reflectances. This is an important step forward for the estimation of daily surface albedo, which plays a key role in water and energy exchanges between surface and atmosphere. At present, surface albedo is usually specified rather crudely as a boundary condition in mesoscale meteorological models and in GCMs. The GCMs generally make use of land cover classification maps such as those produced by *Matthews* [1983]. Each vegetation type is assigned morphological, physiological, and albedo properties from values obtained in the ecological literature. The information brought by POLDER can refine significantly at least the estimate of albedo. An inherent limitation here is that integrations in wavelength over the solar spectrum and in time over the diurnal cycle are required to obtain a daily average of albedo from the measured spectral hemispherical reflectances. Empirical relationships are needed to complete these steps.

Classifications: The directional signature may be thought of as additional channels, which add to the more conventional spectral and temporal information. If it is assumed that the spectral BRDF at the surface is decomposed as a series of n basic bidirectional functions (this is the choice made in the processing line with $n = 3$; see section 4.6), then n different pieces of information are available per spectral band instead of 1 for nondirectional sensors. Thus, in principle, classifications of land cover types can be refined and improved with the directional signature. This is still, however, an exploratory issue. The variability of directional signatures according to the surface type has to be assessed, and the amount of new information brought by these additional variables to be determined.

Vegetation indices: Some thought has been given in recent years to the design of new vegetation indices to minimize various effects (atmosphere, soil reflectance) which disturb the direct interpretation of spectral reflectances in terms of vegetation photosynthetic activity [e.g., *Huete*, 1988; *Kaufman and Tanré*, 1992]. Conversely, it should be possible to use the directional signature to construct new vegetation indices and semiempirical relations between these improved indices and biophysical parameters. Optimal viewing directions may be selected to minimize the effects of soil reflectance and of

residual inaccuracies in the atmospheric correction. For example, *Roujean and Bréon* [1995] have established theoretically a semiempirical relation, independent of vegetation type, between spectral reflectances in a particular viewing configuration, and the daily fraction of absorbed photosynthetically active radiation (PAR).

Inversion: An alternative way of using a directional signature is to attempt its inversion in terms of biophysical parameters, using a model of bidirectional reflectance of the surface. Several authors have elaborated tractable, analytical models of the BRDF, so that they could be inverted against observations [e.g., *Verhoef*, 1984; *Nilson and Kuusk*, 1989; *Jupp and Strahler*, 1991; *Verstraete et al.*, 1990; *Kuusk*, 1994; *Li et al.*, 1995]. Some of these models were effectively inverted against field data [e.g., *Pinty et al.*, 1990; *Deering et al.*, 1992; *Liang and Strahler*, 1994]. Inversion of BRDF models against satellite data is still at a very preliminary stage [*Rahman et al.*, 1993; *Jacquemoud et al.*, 1995]. The accumulation of directional data in short periods of time permitted by the POLDER concept should allow the extraction by inversion of significant information on leaf reflectances, leaf area index, and other structural properties of vegetation canopies. However, the question of the behavior of the inversion process in the general case of heterogeneous pixels has not been addressed yet.

In the context of model inversion, two specific directions are of particular interest, namely, the hot spot and specular directions. The so-called hot spot effect, or opposition effect, that is, the signal enhancement when the Sun and view directions coincide, has received considerable attention [e.g., *Nilson and Kuusk*, 1989; *Jupp and Strahler*, 1991; *Verstraete et al.*, 1990]. The POLDER instrument concept is well adapted to the observation of the hot spot, as was demonstrated during the airborne POLDER campaign on the Boreal Ecosystem-Atmosphere Study (BOREAS) experimental site [*Bréon et al.*, 1997]. The POLDER measurements on ADEOS will offer the first opportunity of systematic and global observations of the hot spot. One may explain the special interest of these measurements by noting that there is a more direct link between radiative properties of canopy elements (leaves, soil) and the observed reflectance in that particular direction, since shadows do not contaminate the observed signal. The width of the hot spot peak is closely related to the structural characteristics of the canopy, such as leaf area index, and ratio (leaf size)/(canopy height) [e.g., *Nilson and Kuusk*, 1989].

Another interesting particular geometry is the specular direction, for which the signal is a function of the surface wetness. This may be particularly interesting for the monitoring of large rice fields of Southeast Asia for example, or of large wetland areas, acting as sources of methane, in boreal regions (V. Vanderbilt, personal communication, 1994). Sharp signatures of the BRDF in the specular direction were obtained from rice fields during the airborne POLDER campaign at the La Crau site in 1991 [*Leroy and Bréon*, 1996].

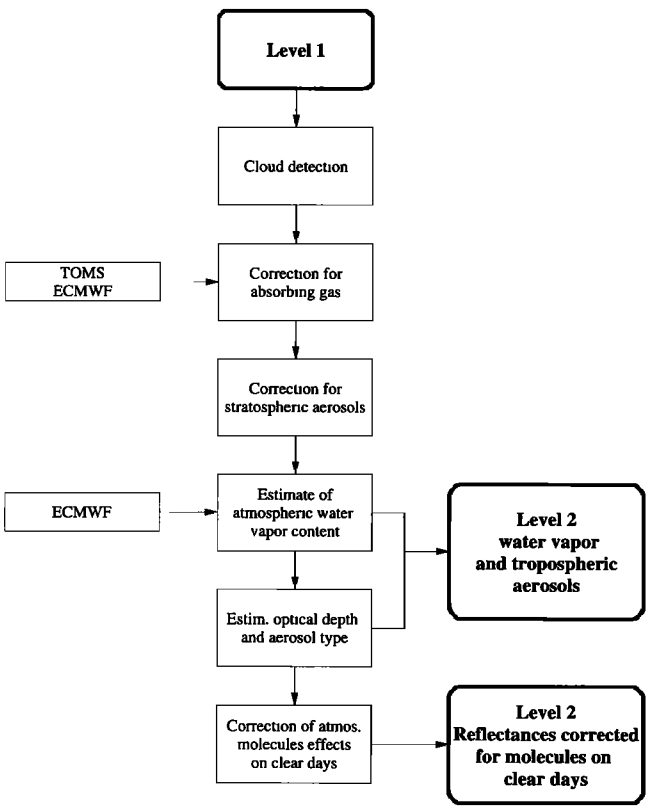

Figure 1a. Flow chart of POLDER data processing in the "land surface and aerosols over land" processing line. From level 1 (TOA geocoded reflectances) to level 2 (geophysical products generated for each orbit).

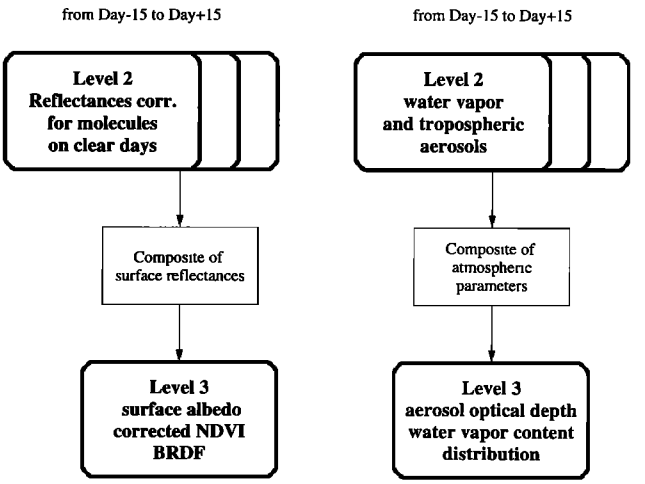

Figure 1b. Same as Figure 1a, but from level 2 to level 3 (global products at 10 days frequency).

4. Description of the Processing Line

4.1. Overview

The processing line "land surfaces and aerosols over land" generates level 2 and 3 products from level 1 products. Here, "level 1" stands for geocoded, calibrated components of the Stokes vector I, Q, U of the radiance field, for the illuminated part of an orbit. "Level 2" and "level 3" stand for geophysical products processed for one orbit and at global scale from a composite of several days of observation, respectively.

Figure 1 shows the overall flow chart of the "land surface and atmosphere over land" processing line. Cloud detection is first applied to the measurements. If the pixel is recognized as clear, a correction for stratospheric aerosols and absorbing gases (O_3, H_2O, and O_2) is applied to the 443-, 670-, 765-, 865-, and 910-nm channels. The inversion of atmospheric parameters (water vapor and aerosol) is applied to the resulting cor-

Table 2. Atmospheric Aerosols and Water Vapor Products

Product	Spatial and Temporal Resolution	Description
Aerosol characteristics and water vapor content	Each orbit (level 2), 3 × 3 POLDER pixels	Aerosol optical thickness at 865 nm Aerosol refractive index (one of three possible values) Aerosol Angström coefficient (one of four possible values) Quality index for aerosol estimate Precipitable water vapor content (g cm^{-2}) Same, as derived by ECMWF Scaled precipitable water vapor, as derived by ECMWF (see text) Quality index for water vapor estimate
Statistical distribution of aerosols and water vapor	Every 10 days (level 3), 3 × 3 POLDER pixels	Number of observations in compositing period (10 days) Histogram of water vapor content Histogram of aerosol optical depth Histogram of Angström coefficients Histogram of aerosol refractive index

rected reflectances, which generates level 2 atmospheric products. An accurate surface reflectance is derived only for nonhazy days: thus, if the retrieved aerosol optical thickness is smaller than a given value, the directional reflectances are corrected for molecular scattering and stored as a level 2 product. These directional reflectances are subsequently used at level 3 in a temporal composition of directional reflectances, which yields spectral hemispherical reflectances and a complete description of the surface BRDF. Level 3 processing also generates temporal statistics on the retrieved atmospheric parameters. Tables 2 and 3 give the detailed content of the level 2 and 3 atmospheric and surface reflectance products. The processing line uses external data from TOMS/ADEOS, for ozone correction, and from the European Centre for Medium-Range Weather Forecasts (ECMWF) for water vapor correction and water vapor retrieval.

4.2. Cloud Detection

Cloud detection is rather difficult with POLDER, in comparison with other instruments such as SPOT, AVHRR, or Meteosat, because of the lack of thermal infrared channels and the rather low spatial resolution. The cloud detection strategy applied to POLDER relies on several complementary principles, as illustrated in Figure 2. The measured reflectance at 670 and 865 nm is first compared to a threshold value. This threshold varies with space and time and has been derived from an analysis of a multiannual global vegetation index (GVI) product. Similarly, the NDVI from the two spectral measurements is compared to a threshold which has the same origin. This test will detect clouds which show a large reflectance contrast with the surface. The ratio of the 763- and 765-nm measurements is then used to derive an estimate of the oxygen pressure of the main reflector. This is possible because these channels are centered on the so-called A oxygen absorption band. This pressure is then compared to the surface pressure derived from a digital elevation model at 15-km resolution. Some uncertainties result from the surface spectral signature, and the test will only detect medium and high clouds. Finally, when such viewing directions are available, the algorithm will analyze the polarized reflectance for scattering angles close to 140°. At these angles, liquid clouds show a large polarized reflectance, which is a clear indication of their presence. This test cannot detect ice clouds, however.

The tests are applied in sequence to the radiometry of any given pixel. It is sufficient that one of the tests be positive to declare the pixel cloudy. All tests are applied, and the result of each test is stored for further quality control. Moreover, if one pixel is declared cloudy after passing the tests, all neighboring pixels are also declared cloudy. The intention is to discard pixels contaminated by cloud shadows and to account for the fact that cloudy areas are generally surrounded by areas with fractional cloud cover. The various cloud tests are described in more detail in the following.

Reflectance and vegetation index thresholds. The principle of this test is to compare the TOA reflectances observed by POLDER, to a reference data base of TOA reflectances depending on space and time. This database of reflectances is

Table 3. Surface Reflectance Products

Product	Spatial and Temporal Resolution	Description
Surface bidirectional reflectances	Each orbit (level 2), full resolution	Viewing/illumination geometry Quality indices Reflectances corrected for atmospheric effects at 443, 670, 765, and 865 nm, for each viewing direction
Hemispherical reflectances and indices	Every 10 days, global (level 3), full resolution	Median sun zenith angle Composited surface hemispherical reflectances at 443, 670, 765, and 865 nm Normalized vegetation index derived from hemispherical reflectances at 670 and 865 nm
Distribution function of bidirectional reflectances	Every 10 days, global (level 3), full resolution	Number of measurements in compositing period Coefficients of BRDF model at 443, 670, 765, and 865 nm Quality indices

derived from AVHRR/GVI data, that is, weekly composites of AVHRR global area coverage (GAC) reflectance data in the visible and near-infrared at 15-km resolution. The need for a database ready at launch made it necessary to use AVHRR observations rather than those of POLDER. Five years of GVI data are used to generate the threshold base. The GVI data are processed as described by *Bouffiès and Bréon* [1996] with the objective to eliminate cloudy GVI data and to allow interannual variability in the reference data set. The GVI data temporal resolution has been reduced to 1 month.

The test is not applied when the ECMWF meteorological field indicates snow coverage. Among the available measurements for a pixel, the observation with the lowest viewing zenith angle is selected, in order to reduce the influence of bidirectional effects. Finally, if the reflectances R_{670} or R_{865} (or the NDVI derived from R_{670} and R_{865}) are significantly larger (lower) than the corresponding quantities of the database, then the pixel is declared cloudy.

O_2 apparent pressure. The apparent pressure P_{app} is derived from POLDER measurements as

$$P_{app} = P_0\left(\frac{A \exp(-\beta X) + G(m, X)}{m}\right)^{1/2} \quad (1)$$

where P_0 is the standard pressure (1013 hPa), m is the air mass factor,

$$G(m, X) = \sum_{i=0}^{2}\sum_{j=0}^{2} a_{ij} m^i X^j, \quad (2)$$

$$X = \frac{(R_{TOA} - R_{mol})_{763}}{(R_{TOA} - R_{mol})_{765}}. \quad (3)$$

R_{mol} is the precomputed reflectance due to molecular scattering, and β and a_{ij} are known numerical coefficients. Relations (1) and (2) have been derived by *Bréon and Bouffiès* [1996] on the basis of radiative transfer calculations. When taking into account the instrumental noise and errors due to variable aerosol loading, the expected accuracy of apparent pressure estimate is of the order of 100 hPa [*Bréon and Bouffiès*, 1996]. If the apparent pressure is significantly smaller than the surface pressure expected in clear conditions, the pixel is declared cloudy.

Polarization signature near the rainbow direction. The polarized phase function of water droplets shows a large maximum for a scattering angle of 140° (direction of the rainbow). Therefore polarized radiance measurements allow an accurate detection of liquid clouds, as was shown with airborne POLDER measurements [*Goloub et al.*, 1994]. The test will analyze the directional signature of the polarized reflectance in directions close to the 140° scattering angle. The test will declare a pixel cloudy if a local maximum is observed in the predicted direction. The major limitation of this test, apart from the case of ice clouds, is the availability of the needed viewing geometry among POLDER observations of the pixel. Figure 3 shows a simulation of the range of available scattering angles that will be observed by POLDER for several northern latitudes at a given date (March 21). This range varies as expected both with latitude and with the off-nadir viewing angle in the across-track vertical plane. The pattern of figures such as that of Figure 3 is roughly symmetrical with respect to the Equator. If a date other than the equinox is chosen, the pattern of figures is translated in latitude but not substantially modified. Figure 3 and other similar figures show that about 60% of observed pixels satisfy the requirement of availability of 140° scattering angles.

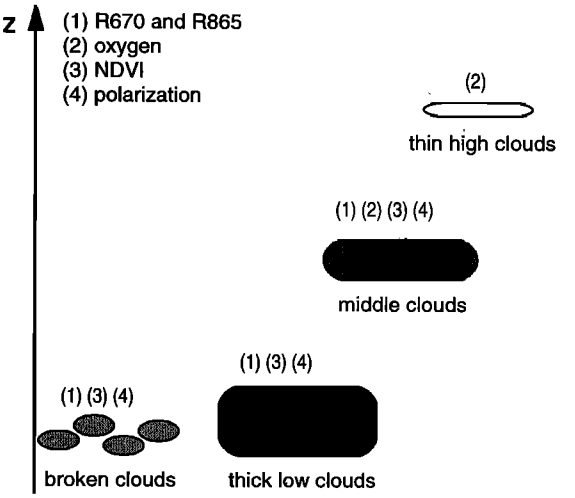

Figure 2. Type of clouds that are expected to be detected by each of the tests of cloud detection.

The three tests described above involve a series of thresholds which are yet to be determined, and which will be tuned during the validation phase after launch. This validation phase will also permit one to assess the accuracy of cloud screening once the thresholds are optimally tuned. Several sources of errors may be listed. The test involving a database of reflectances and vegetation indices will not be able to account for interannual variability phenomena. The bands of the AVHRR/GVI database are not identical to those of POLDER. This latter drawback can be corrected in a later stage of the processing line, by replacing the AVHRR/GVI database by a database derived from POLDER itself. Subpixel fractional cloud cover will be difficult to detect with any of the implemented tests.

4.3. Correction for Stratospheric Aerosol Effects and Gaseous Absorption

The stratospheric aerosol correction module is planned to handle the case of a large aerosol emission, such as those from the El Chichon or the Pinatubo volcanoes in the recent past. It is assumed that a few months have passed since the eruption, so that the stratospheric aerosols have a low influence on the signal, and may be considered zonally distributed. The optical thickness used as a function of latitude can be regularly updated from various sources, such as the Stratospheric Aerosol and Gas Experiment (SAGE) or the existing sunphotometer or lidar network. For this correction, single scattering is assumed. The prescribed aerosol phase function will be derived from the SAGE experiment according to the method of *Brogniez et al.* [1996].

Compared to other optical instruments such as AVHRR, POLDER has relatively narrow bands (between 10 and 40 nm; see Table 1) which have been chosen to minimize gas absorption. Except for the 763-, 765-, and 910-nm channels, which are used as atmospheric probes, gas absorption is relatively weak (see Table 4), and the correction to be applied is small. The stratospheric ozone column abundance U_{O_3} (cm atm) will be provided by the total ozone mapping spectrometer (TOMS)

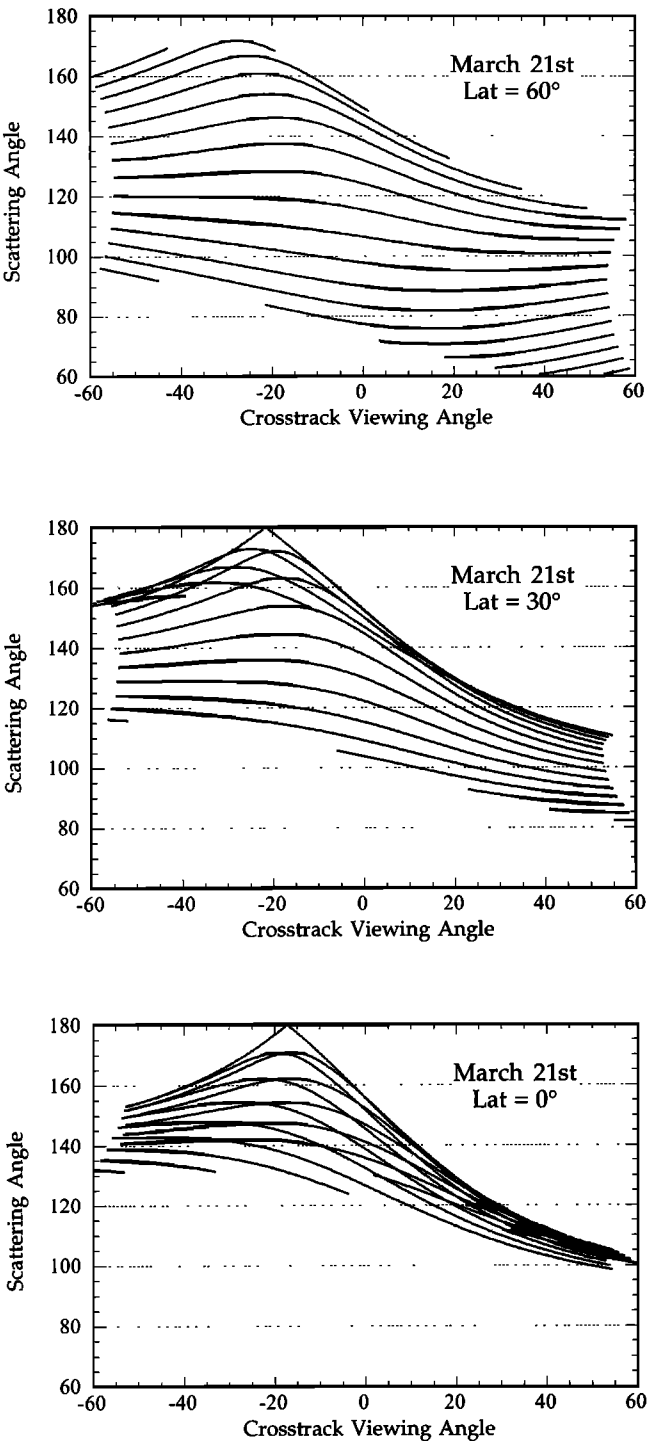

Figure 3. Simulated range of available scattering angles acquired on one pass, as a function of the off-nadir viewing angle in the across-track vertical plane, on March 21, for latitudes 60°N, 30°N, and 0°.

instrument also onboard ADEOS along with POLDER. If, for some reason, TOMS/ADEOS measurements are not available, grided data derived from ECMWF meteorological field can be used with a reasonable accuracy. The transmission of ozone T_{O_3} is precalculated as a polynomial function of mU_{O_3}. This precalculation is derived from simulations using a line-by-line model [*Scott*, 1974]. The correction then is simply written

$$R_{corr} = R_{meas}/T_{O_3} \quad (4)$$

This simple formulation is possible because the main ozone layer is located well above the scattering layers. A formulation similar to (4) is used for the water vapor correction; however, the transmission T_{H_2O} is not a direct transmission but a total (direct + diffuse) transmission approximated for each viewing direction by a second-order polynomial of the R_{910}/R_{865} ratio, the coefficients of which do not depend on the viewing direction.

A particular treatment concerns the 763- and 765-nm channels. The reflectance $R_{765,corr}$ that would be measured if there was no absorption is assumed to be the same in both channels. The wide band (centered at 765 nm) can be decomposed into one part including the narrow band (centered at 763 nm), which is strongly affected by the O_2 line absorption, and another one only affected by weak O_3 and H_2O absorptions. Therefore the R_{763} and R_{765} measured reflectances are linked by [*Parol et al.*, 1994]

$$R_{765} = AR_{763} + (1 - A)R_{765,corr}T_{H_2O}T_{O_3}, \quad (5)$$

where A is a constant close to 0.3, which was derived from line-by-line simulations. The ozone transmission T_{O_3} is parameterized as a function of mU_{O_3}, while the water vapor transmission T_{H_2O} is parameterized as above as a polynomial of the R_{910}/R_{865} ratio. Then the reflectance $R_{765,corr}$ is derived from R_{763} and R_{765} measurements by using (5).

4.4. Tropospheric Aerosols

The physical rationale of the algorithm is described in detail by *Herman et al.* [this issue]. The following concentrates on the practical aspects of the algorithm implementation. The algorithm is based on the comparison between polarized radiances, measured at 443, 670, and 865 nm, and precalculated values. The input polarized radiances are those corrected for stratospheric aerosols and gaseous absorption, spatially averaged on areas of size 3 × 3 pixels. The spatial average reduces misregistration effects between the measurements taken by each individual polarizer in the POLDER instrument. These misregistration effects are more critical with polarized radiances than with simple radiances, since the Stokes components U and Q, and also the polarized radiance L_{pol} involve differences between the radiance measurements (in general much larger than U or Q) taken by the polarizers. A slight surface heterogeneity, coupled to misregistration effects, induces some noise in the evaluation of such differences, which can be reduced with sufficient averaging.

Table 4. Typical Values of Gaseous Absorption in the POLDER Channels Used in the "Land Surface and Atmosphere Over Land" Processing Line

Channel, nm	Ozone Absorption, %	Oxygen Absorption, %	Water Vapor Absorption, %
443	0.3	0	0.0
670	4.5	0	1.5
763 (narrow)	0.6	41.6	1.4
765 (wide)	0.6	12.4	2.2
865	0.0	0	2.7
910	0.0	0	31.1

These values correspond to a twofold path through the U.S. standard atmosphere, with an air mass factor of 3.

Following the discussion of section 3.1, the measured polarized radiance L_{pol} is modeled as

$$L_{pol} = L_{pol,aer} + L_{pol,Ray} + L_{pol,surf}, \quad (6)$$

that is, the sum of three contributions: (1) $L_{pol,aer}$, generated by aerosol scattering, (2) $L_{pol,Ray}$, by Rayleigh scattering, and (3) $L_{pol,surf}$ due to the reflection of sunlight by the surface, attenuated by the atmospheric transmission on the downwelling and upwelling paths. These terms are expressed as

$$L_{pol,aer}(\lambda, \theta_s, \theta_v, \phi) = \frac{\tau_a(\lambda, \alpha)}{4 \cos \theta_v} \frac{E_s}{\pi} Q_a(\lambda, \Theta, n, \alpha), \quad (7)$$

$$L_{pol,Ray}(\lambda, \theta_s, \theta_v, \phi) = \frac{\tau_m(\lambda)}{4 \cos \theta_v} \frac{E_s}{\pi} Q_m(\lambda, \Theta), \quad (8)$$

$$L_{pol,surf}(\lambda, \theta_s, \theta_v, \phi) = \cos \theta_s \frac{E_s}{\pi} R_{pol,surf} \cdot \exp\left[-[c_1(\lambda, \alpha)\tau_a(\lambda, \alpha) + c_2(\lambda)\tau_m(\lambda)]\left(\frac{1}{\cos \theta_s} + \frac{1}{\cos \theta_v}\right)\right]. \quad (9)$$

In (7)–(9), $\tau_a(\lambda, \alpha) = (\lambda/865)^{-\alpha}\tau_{a865}$ and $\tau_m(\lambda)$ are the optical thicknesses of the aerosols and of the molecules, respectively. Here, $\tau_m(\lambda)$ is calculated according to the surface altitude provided by a coarse-resolution digital elevation model. E_s is the TOA solar irradiance. $Q_a(\lambda, \Theta, n, \alpha)$ and $Q_m(\lambda, \Theta)$ are precalculated functions, which depend on the geometric angles θ_s, θ_v, ϕ only through the scattering angle Θ. Equations (7) and (8) are in the classical form corresponding to primary scattering approximation, but Q_a and Q_m are not just the polarized phase functions for aerosols and molecules. In order to account crudely for multiple scattering effects, Q_a and Q_m are calculated as follows. For an average solar zenith angle $\theta_s = 45°$, the TOA polarized radiance L_{pol} is calculated for each aerosol model, for each wavelength, and for the range of θ_v and ϕ covering the POLDER field of view. The calculations are performed for the case of a black ground (so that $L_{pol} = L_{pol,aer} + L_{pol,Ray}$) and for $\tau_{a865} = 0$ and $\tau_{a865} = 0.20$. Then $Q_a(\lambda, \Theta, n, \alpha)$ and $Q_m(\lambda, \Theta)$ are adjusted so that (6)–(8) provide the best adjustment of the results. $Q_m(\lambda, \Theta)$ is very close to the molecule polarized phase function for $\lambda = 670$ and 865 nm, but differs substantially from it at 443 nm, where single scattering is no longer a good approximation. The functions c_1 and c_2 may also be precalculated. At present, we just use $c_1 = 0$ and $c_2 = 1$.

The aerosol size distributions have been chosen as power laws, so that Q_a depends on the refractive index n and Angström coefficient α of aerosols. The precalculation of Q_a is made at 443, 670, and 865 nm for 12 aerosol models, which at present, are characterized by $n = 1.33, 1.40, 1.50$, and $\alpha = 0.5, 1.0, 1.5, 2.0$. The choice of this discretization of n and α results from simulations of aerosol retrieval from the polarization signal [*Herman et al.*, this issue]. Note that the chosen models correspond to nonabsorbing aerosols. The choice of aerosol models will be updated in later stages of the processing line.

$R_{pol,surf}$ models the polarized reflectance of the surface. Following the hypothesis that the polarized reflectance is generated by specular reflectance at the surface, it is considered spectrally neutral. It is modeled for bare soils as [*Bréon et al.*, 1995]

$$R_{pol,surf}(\Theta) = \frac{F_P[(\pi - \Theta)/2]}{4 \cos \theta_s \cos \theta_v}, \quad (10)$$

and for vegetated areas as [*Rondeaux and Herman*, 1991]

$$R_{pol,surf}(\Theta) = \frac{F_P[(\pi - \Theta)/2]}{4(\cos \theta_s + \cos \theta_v)}, \quad (11)$$

where $F_P(\gamma)$ is the polarized Fresnel reflection coefficient for an incidence angle γ. In practice, the surface polarized reflectance is a weighted sum of (10) and (11), with weighting coefficients derived from an evaluation of the NDVI, averaged over the available viewing directions.

Equation (6) is solved for the unknown τ_{a865}, for each of the 12 aerosol models, for each available scattering angle, and for each of the three wavelengths 443, 670, and 865 nm. For each aerosol model, an average and a dispersion of the resulting values of τ_{a865} are calculated. The retrieved aerosol model is that which minimizes this dispersion, and the retrieved τ_{a865} is the average τ_{a865} associated to this aerosol model.

A series of tests is made to secure this calculation. First, the aerosol model is retrieved only if the maximum scattering angle is large enough (typically larger than 140°) because the signal is sensitive to this parameter mainly in the backscattering region. The quality of the results is expected to improve as the available range of scattering angles increases [*Herman et al.*, this issue]. Figure 3 shows that for the particular date of March 21, the range of variations is about 60°–80° at latitude 60°N, is always less than 40° at the Equator, and even less than 10° at this latitude in the eastward part of the orbit. As mentioned earlier, if a date other than the equinox is chosen, the pattern of figures is translated in latitude. Thus some periods and latitudes are more favorable than others for aerosol model inversion.

Moreover, over vegetated pixels (nearly black at 443 nm), characterized by high NDVI values, a test is made to verify the consistency between the measured TOA reflectance at 443 nm and the modeled TOA reflectance:

$$R_{model,443} = \frac{\tau_a(443, \alpha)P_a(443, \Theta, n, \alpha) + \tau_m(443)P_m(\Theta)}{4 \cos \theta_s \cos \theta_v}, \quad (12)$$

where P_a stand for the aerosol phase function computed with the retrieved values of n and α, and P_m for the molecule phase function. The aerosol model and optical thickness will not be retrieved if these two quantities differ too much.

4.5. Precipitable Water Vapor

The precipitable water vapor content U_{H_2O} (g cm^{-2}) is derived for each viewing configuration from a precalculated relation between U_{H_2O} and R_{910}/R_{865}. This relation proceeds from simulations of radiative transfer in an absorbing and scattering atmosphere, where the atmospheric absorption coefficient of water vapor is obtained with line-by-line simulations [*Bouffiès et al.*, 1995]. The most important sources of errors are expected to originate from the coupling between water vapor absorption and atmosphere scattering by molecules and aerosols, and from the spectral variations of the surface reflectance between 865 and 910 nm.

Figure 4 is a scatter plot of mU_{H_2O} as a function of the ratio R_{910}/R_{865}, obtained from simulations made for five different atmospheric profiles (World Meteorological Organization), 14 different surface spectra, and a large number of observation

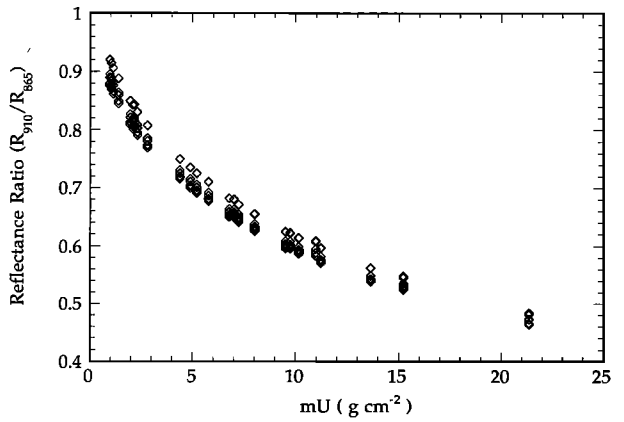

Figure 4. Ratio R_{910}/R_{865} as a function of mU_{H_2O} for 14 different surface types and five atmospheric profiles.

geometries. Figure 4 shows that the dispersion of results for various atmosphere and surface conditions is weak and yields an estimate of 10% accuracy for water content retrieval. From simulations such as those of Figure 4, an analytical relation between R_{910}/R_{865} and U_{H_2O} can be derived [*Bouffiès et al.*, 1995].

Some uncertainty results from the atmospheric vertical profile. This is because water vapor absorption, in the POLDER spectral bands, depends not only on the water vapor amount, but also on the temperature T and pressure P of the layer. Thus the equation derived from Figure 4 relates R_{910}/R_{865} with a scaled amount defined by

$$U^*_{H_2O} = \int_0^{P_{surf}} \frac{q(P)}{g} \left(\frac{P}{P_0}\right)^m \left(\frac{T_0}{T}\right)^n dP \qquad (13)$$

where $q(P)$ is the vertical profile of the water vapor mixing ratio and (m, n) are two numerical coefficients close to (0.9, 0.4). A knowledge of the vertical profile can be derived from grided analyses, such as those of ECMWF. The estimated scale amount $U^*_{H_2O}$ can then be used to retrieve the integrated water vapor content U_{H_2O}:

$$U_{H_2O} = U^*_{H_2O} \frac{U^{ECMWF}}{U^{ECMWF}_{scaled}} \qquad (14)$$

where U^{ECMWF} is the total water vapor amount estimated by the operational weather center, and U^{ECMWF}_{scaled} is derived from its vertical profile, as in (13). The need for knowledge of the water vapor vertical profile for a retrieval of the total water vapor amount may seem paradoxical. It should be understood, however, that the vertical profile data are only used to provide a correction to the first estimate, the magnitude of which does not exceed a few percent.

The values obtained over all viewing configurations are then averaged to get the final precipitable water content. The dispersion of water content when the viewing angle varies is used to derive a quality indicator for that product. As for aerosols, the estimation of precipitable water is made on a grid of resolution 3 × 3 pixel, for each orbit segment. A statistical distribution of water vapor content is also produced at a global scale, at the same resolution, with a period of 10 days (see Table 2).

4.6. Surface Directional Signature and Hemispherical Reflectances

A two-step procedure is needed to acquire a complete surface BRDF. The first step is a correction for molecular scattering in order to get bidirectional reflectances at the surface level. The second is a compositing technique which uses surface reflectances acquired on each pixel over a 1-month compositing period.

Corrections for molecular scattering. A correction for molecular scattering is performed for each pixel and for the 443-, 670-, 765-, and 865-nm wavelengths whenever (1) the aerosol optical depth τ_{a865} acquired in a previous step (section 4.4) has been retrieved with sufficient confidence, (2) it satisfies $\tau_{a865} < 0.3$, and (3) the ratio of the aerosol reflectance to the surface reflectance is low enough for each wavelength. A correction for aerosol effects has not been implemented at this stage, although it should be feasible in principle, since both optical depth and aerosol phase function are available (see section 4.3). It will be implemented after the aerosol product has been fully validated. This protocol gives, however, some insurance that pixels with large aerosol loading will effectively be removed.

The correction scheme assumes that (1) no tropospheric aerosols are present and (2) the effects of molecular scattering are not coupled with those of stratospheric aerosols and absorbing gases. The relation between the corrected reflectance $R_{surf}(\lambda, \theta_s, \theta_v, \phi)$ and the reflectance at the top of the molecular layer $R(\lambda, \theta_s, \theta_v, \phi)$, that is, the TOA reflectance corrected for stratospheric aerosols and absorbing gases (see section 4.2), is classically that of the 5S code [*Tanré et al.*, 1990]:

$$R(\lambda, \theta_s, \theta_v, \phi) = R_{mol}(\lambda, \theta_s, \theta_v, \phi) + R_{surf}(\lambda, \theta_s, \theta_v, \phi) \cdot \frac{T(\theta_s)T(\theta_v)}{1 - R_{surf}(\lambda, \theta_s, \theta_v, \phi)s(\lambda)} \qquad (15)$$

where $s(\lambda)$ is the spherical albedo of the molecular atmosphere, $T(\theta)$ its transmission on a path of incidence angle θ, and R_{mol} is the reflectance of the molecular layer for a black underlying surface. The latter three quantities are precalculated for discrete values of wavelength, geometric angles, and surface altitude, and interpolated to account for actual values of geometric angles and surface altitude as given by a digital elevation model. Equation (15) is then solved for R_{surf}.

There are two main sources of inaccuracy in this correction. The first, already pointed out, is the lack of correction for aerosol effects. This may yield errors ΔR of the order of 0.01

Table 5. TOA Reflectances Over a Black Surface Due to the Molecules Only, and Due to Molecules + Aerosols, in the Case of a Visibility of 23 km and a Sun Zenith Angle Equal to 45°, at Nadir Viewing (evaluation with 5S)

	Channel			
	443 nm	670 nm	765 nm	865 nm
R molecules	0.088	0.017	0.009	0.006
R molecules + aerosol	0.11	0.030	0.020	0.015
ΔR	0.022	0.013	0.011	0.009

Aerosols are of the continental type. The differences ΔR between the two lines are also shown.

or more, as shown in Table 5. The second is that (15) assumes a Lambertian surface: this correction scheme assumes that all downward photons from diffuse sky radiation are reflected with the same efficiency R_{surf}, irrespective of their incidence angle. Also, photons eventually reaching the sensor, which have been at least once reflected by the surface and scattered by the atmosphere, are also reflected with the same efficiency R_{surf}. The error resulting from this approximation has been evaluated by simulation. The TOA bidirectional reflectance corresponding to various atmospheric conditions and various surface angular signatures has been computed using the 6S code [*Vermote et al.*, 1996], which accounts for bidirectional effects of the surface. From the resulting TOA reflectances, the surface reflectances have been derived from (15), and the differences (errors) between resulting and original surface BRDF have been calculated. Figure 5 shows examples of original surface BRDF and associated errors in a few particular cases. The errors increase with aerosol loading and Sun and view zenith angle. They can reach a few 0.01 in typical situations in the near infrared, as shown by Figure 5, and typically 0.002–0.006 over vegetated areas in the visible. The errors tend to smooth out the directional signature. They are not negligible, and a better atmospheric correction taking into account explicitly the surface BRDF should be implemented in a later stage of the processing line.

Compositing technique. The compositing technique describes the surface bidirectional reflectance, averaged over a sliding compositing period of 30 days, with a limited number of model parameters. The period of production of the composite is 10 days. The compositing process has a twofold objective: first, to collect a sufficient number of directional data to constrain the adjustment of the BRDF model and, second, to smooth the time profiles of reflectances to reduce effects of instrumental noise, inaccuracies in cloud detection or atmospheric correction algorithms, or natural variability of the surface. For this purpose, time series of atmospherically corrected reflectances, acquired during a period of composition, are fitted with a parameterized BRDF model:

$$R_{surf}(\lambda, \theta_s, \theta_v, \phi) = f(k_0(\lambda), k_1(\lambda), \cdots, k_n(\lambda); \theta_s, \theta_v, \phi). \quad (16)$$

Here f is an analytic, nondivergent function on the domain of possible geometric angles, satisfying the property of reciprocity when inverting the solar and viewing directions. The coefficients k_n are wavelength dependent and are retrieved as the products of the fitting procedure. These coefficients permit the deduction of the reflectance for any geometry of Sun or view observation, and thus also an estimate of spectral hemispherical reflectances.

The choice of the BRDF model is a serious problem. Many explicit analytic models of the surface BRDF exist in the literature. They are either linear or nonlinear, and either empirical [*Walthall et al.*, 1985; *Shibayama and Wiegand*, 1985; *Goel*, 1988], semiempirical [*Deering et al.*, 1990; *Roujean et al.*, 1992b; *Rahman et al.*, 1993], or physically based (see the Inversion subsection in section 3.3). The model complexity increases with their degree of physical realism.

For the sake of simplicity and computer time limitations, only linear models have been considered here. A detailed comparison of several linear models available in the literature was undertaken to select one operational algorithm. Those considered were (1) the four-parameter empirical model of

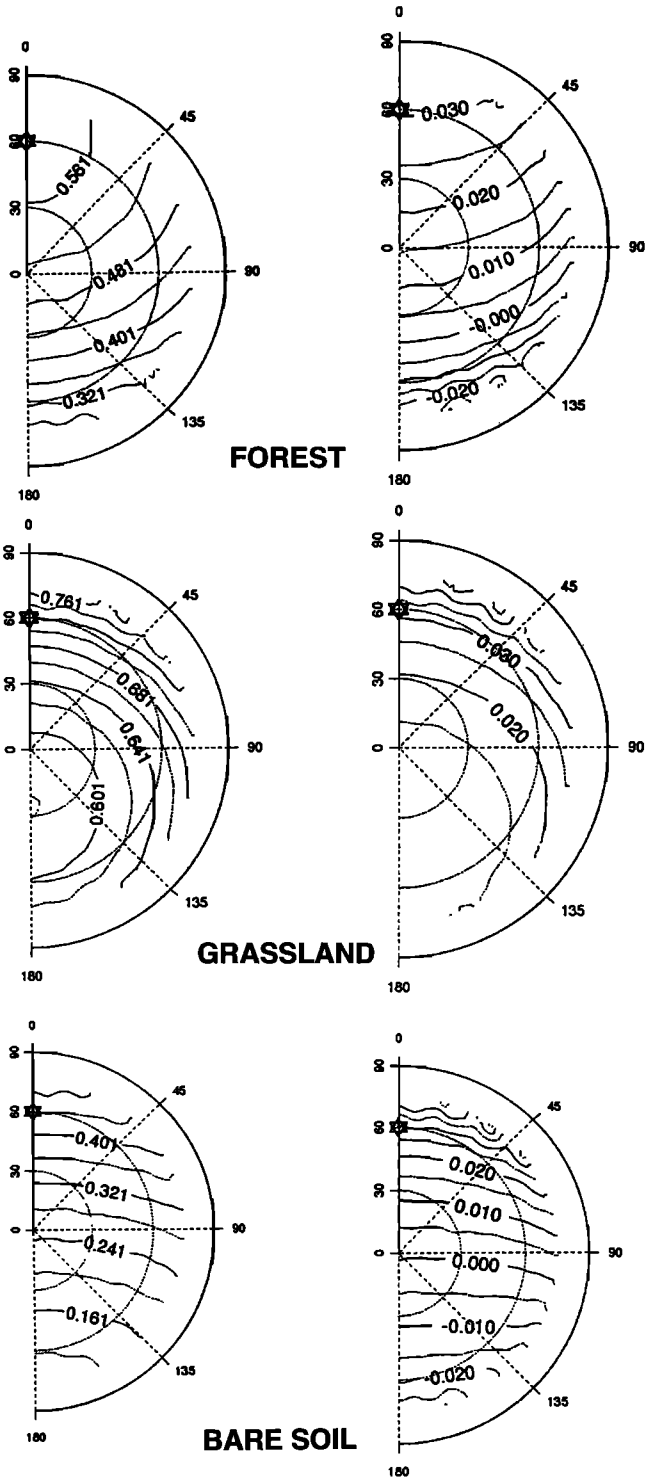

Figure 5. Representation, in polar coordinates, of (left) the surface BRDF and (right) the corresponding error in reflectance units made when the atmospheric correction is applied assuming a Lambertian surface, at 850 nm, for three different surface types: (top) forest cover, (middle) grassland, and (bottom) bare soil. The aerosol optical depth is 0.2 at 550 nm; aerosols are of the continental type. The Sun zenith angle is 60°. The radius represents viewing zenith angle, the polar angle the relative azimuth between the Sun and view directions.

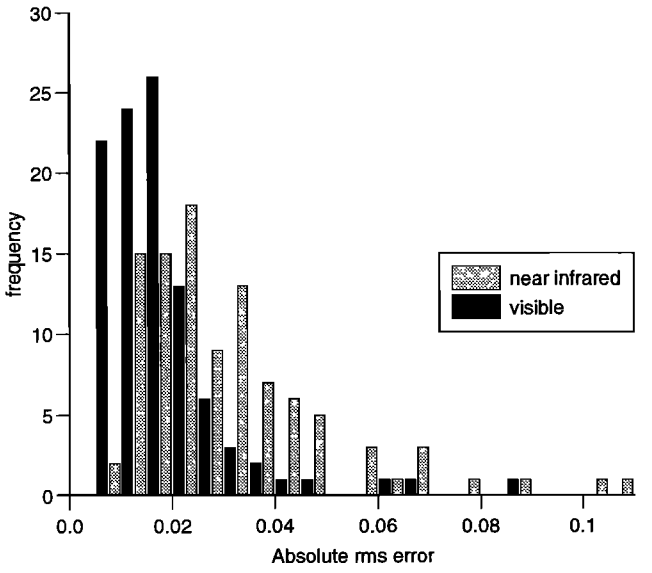

Figure 6. Histogram of absolute rms errors in units of reflectance when applying Roujean et al.'s model to the database of BRDF measurements, in the visible and the near infrared.

Shibayama and Wiegand [1985], (2) a modified version of the four-parameter empirical model of *Walthall et al.* [1985] satisfying the reciprocity principle, as used by *Nilson and Kuusk* [1989], (3) the semiempirical model of *Deering et al.* [1990]; only the part of the model describing the reflectance of a bare soil and including three free parameters was used (the complete formulation of the model is not linear), (4) the three-parameter semiempirical model of *Roujean et al.* [1992b], and (5) a linear decomposition of the BRDF on a basis of spherical harmonics, also referred to as Legendre polynomials [*Goel*, 1988]. Spherical harmonics are functions of only two variables (say, θ_v and ϕ), whereas functions of the three geometric angles are needed. Thus the model with Legendre polynomials was modified to become a reciprocal function of all three geometric angles.

These various models were tested over a variety of field data, available in free-access databases, acquired by various authors, on many different surface types: lava flow, cobble, sand, plowed soils, Kansas prairie, grass, cultures (soybean, wheat, orchard, corn), and spruce and pine forests. Altogether, a set of about 100 BRDF measurements were considered in the analysis, acquired over 18 different types of surfaces, with various Sun zenith angles for each site.

The models were evaluated on the basis of several criteria: (1) ability to fit BRDF measurements acquired at a given Sun zenith angle, (2) ability to fit BRDF measurements acquired with a range of Sun zenith angles (variations of the order of 20°) representative of the variations of θ_s encountered in a 1-month period of POLDER acquisitions, (3) ability to simulate spectral directional hemispherical reflectances (the bidirectional reflectance integrated over the half space of possible viewing directions), for data sets which provided this information, (4) robustness, measured as the dispersion of the retrieved $k_0(\lambda)$ when θ_s varies (for a given surface) over the whole range of available Sun angles, or when some data occupying part of the available directional space are discarded. The latter criterion is particularly important, since it measures the ability to extrapolate a model to Sun or view angles which have not been used to retrieve the model parameters in the fitting procedure.

This evaluation, the details of which are described elsewhere [*Hautecoeur and Leroy*, 1996], leads to the selection of the *Roujean et al.* [1992b] model for the compositing technique. Figure 6 represents a histogram of the rms residual error obtained when applying the model of *Roujean et al.* [1992b] to the complete field data set, and shows that this error (expressed in reflectance) is, on average, 0.01 in the visible and 0.025 in the near infrared. The overall shape of the BRDF is well reproduced by the model, except for the hot spot and specular directions. Thus the directional signature produced at level 3 will not be adequate for inversion of the BRDF in terms of biophysical parameters of the surface if the features of hot spot and specular reflection are of any importance in the inversion process. However, Figure 7 shows that the model reproduces satisfactorily hemispherical reflectances, an important step for the estimation of surface albedo.

The retrieval of the k_i parameters from the observations is a three-step process. A linear regression is first applied, from which a rms error is computed. Measurements where distance to the model is larger than twice this error are eliminated. A second regression is then applied to the remaining observations, from which the final directional signature is retrieved. The elimination of the observations which greatly differ from the bulk directional behavior is done to correct for instrumental noise, or inaccuracies of cloud detection and atmospheric corrections. Similar techniques have been tested on AVHRR data [*Leroy and Roujean*, 1994; *Wu et al.*, 1995]. The technique accuracy with AVHRR data is limited by the fact that only a small fraction of directional space is observed by AVHRR. The accuracy is expected to be much higher with POLDER, which provides much better sampling of directional space, as mentioned earlier. The technique turns out to operate satisfactorily on the airborne POLDER measurements acquired during the La Crau campaign [*Leroy and Bréon*, 1996].

Finally, spectral hemispherical reflectances are computed by

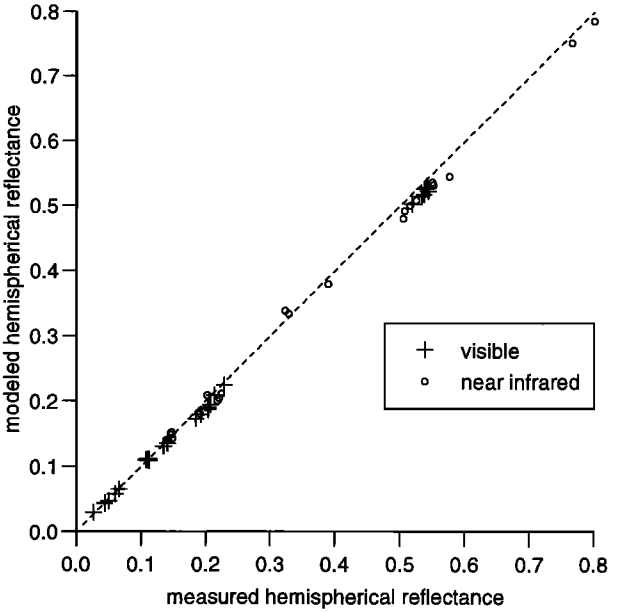

Figure 7. Comparison of observed hemispherical reflectances and those reconstructed with Roujean et al.'s model in the red and near-infrared bands.

integrating the BRDF over the 2π steradian half space of viewing directions, according to the formulae recommended by *Roujean et al.* [1992b]. In this calculation, the Sun zenith angle is taken equal to the median of all Sun zenith angles associated to every orbit pass in the compositing period. Hemispherical reflectances could be derived at another Sun zenith angle using the retrieved k_i. The procedure of integration over viewing angles can induce some error, since the BRDF model is not well defined for zenith angles larger than about 60° (due to the absence of treatment of mutual shadowing in its geometric kernel). Figure 7 shows that this error is necessarily small. This error was further investigated by comparing hemispherical reflectances, first, computed as above and, second, computed assuming that the BRDF for $60° \leq \theta_v \leq 90°$ is equal to that for $\theta_v = 60°$ (a crude but reasonable assumption). The experimental data set on which this comparison was performed was a series of BRDF measurements on various types of surfaces (bare soils, cultures, forests) quoted in the work by *Roujean et al.* [1992b]. Results show that the absolute differences between the two cases are on average 0.004 and 0.006, and at maximum 0.01 and 0.02, for the visible and near-infrared bands, respectively. These errors are not negligible but are of sufficiently low magnitude to consider that the integration procedure is valid.

5. Conclusion

This paper has outlined the benefit that can be expected from POLDER data for the exploration of several important science fields related to atmospheric and land surface properties. It has described in some detail the algorithms which are currently implemented in an operational processing line focusing on the characterization of aerosols and water vapor over land, and on the description of the BRDF of the land surface.

Improvements in the processing line are foreseen after a few years of experience with actual POLDER data. For example, the atmospheric correction procedure should include a correction for aerosol scattering after the aerosol product has been fully validated. The choice of the aerosol models, presently nonabsorbing and with a Junge-type distribution, should evolve toward a choice of aerosol models more representative of the aerosol climatology. An iterative scheme could also be implemented to account for surface directionality in the atmospheric correction. Improvements of the compositing procedure for obtaining the directional signature of the surface are likely. Also, beyond the production of radiative quantities such as the surface BRDF, the new signatures and improved corrections provided by POLDER should lead to the definition of new products, such as the leaf area index or the fraction of absorbed photosynthetically active radiation, in parallel to similar products derived presently from AVHRR [*Sellers et al.*, 1994] or which will be derived from MODIS [*Running et al.*, 1994].

The validation of aerosol and water vapor products will be carried out with a network of sunphotometers located at various places in the world, as described in detail by *Bréon et al.* [this issue]. Cloud detection efficiency will be checked using simultaneous measurements acquired by the worldwide network of meteorological synoptic stations, and by sensors onboard the ADEOS platform having a better resolution, such as ocean color and temperature scanners (OCTS) and advanced visible and near infrared radiometer (AVNIR). The verification of the surface BRDF products provided by POLDER is not straightforward. One possibility is to make POLDER measurements of the BRDF on some specific desert sites [*Cosnefroy et al.*, 1996], adapted to calibration purposes, and on which there is an a priori quantitative knowledge of the shape and magnitude of the BRDF. These sites, however, are characterized by a very high temporal stability of optical properties of their surface + atmosphere system. A verification of the BRDF on sites with high atmospheric and surface variabilities should also be attempted. Possibilities, yet to be explored, could be to compare the BRDF acquired by POLDER and by other sensors such as MODIS or multiangle imaging spectroradiometer (MISR), or by the airborne POLDER on specific sites, characterized by a reasonable spatial homogeneity.

Acknowledgments. This work was supported by Centre National d'Etudes Spatiales and Centre National de Recherches Scientifiques. The authors acknowledge a careful reading of the manuscript by A. Lifermann and J. Perbos from CNES Toulouse, and thank F. Parol and B. Lafrance (LOA Lille), L. G. Liberti (LMCE), and N. Boichis (CESBIO Toulouse) for their contributions to the algorithmic development.

References

Ba, M. B., P. Y. Deschamps, and R. Frouin, Error reduction in NOAA satellite monitoring of the land surface vegetation during FIFE, *J. Geophys. Res.*, *100*(D12), 25,537–25,548, 1995.

Bouffiès, S., and F. M. Bréon, A multiyear composite of GVI data as a clear reflectance database, *Int. J. Remote Sens.*, *17*, 1711–1726, 1996.

Bouffiès, S., D. Tanré, F. M. Bréon, and P. Dubuisson, Atmospheric water-vapor estimate with a differential absorption technique with the POLDER instrument, Proceedings of the Conference on Satellite Remote Sensing II, *Proc. SPIE Int. Soc. Opt. Eng.*, *2582*, 131–143, 1995.

Bréon, F. M., and S. Bouffiès, Land surface pressure estimate from measurements in the oxygen A absorption band, *J. Appl. Meteorol.*, *35*, 69–77, 1996.

Bréon, F. M., D. Tanré, P. Leconte, and M. Herman, Polarized reflectance of bare soils and vegetation: Measurements and models, *IEEE Trans. Geosci. Remote Sens.*, *33*, 487–499, 1995.

Bréon, F. M., V. Vanderbilt, M. Leroy, P. Bicheron, C. L. Walthall, and J. E. Kalshoven, Evidence of hot spot directional signature from airborne POLDER measurements, *IEEE Trans. Geosci. Remote Sens.*, in press, 1997.

Bréon, F. M., J. L. Deuzé, D. Tanré, and M. Herman, Validation of spaceborne estimates of aerosol loading from Sun photometer measurements with emphasis on polarization, *J. Geophys. Res.*, this issue.

Brogniez, C., J. Lenoble, M. Herman, P. Lecomte, and C. Verwaerde, Analysis of two balloon experiments in coincidence with SAGE II, in case of large stratospheric aerosol amount: Post-Pinatubo period, *J. Geophys. Res.*, *101*(D1), 1541–1552, 1996.

Charlson, R. J., S. E. Schwartz, J. M. Hales, R. D. Cess, J. A. Coakley, J. E. Hansen, and D. J. Hoffman, Climate forcing by anthropogenic aerosol, *Science*, *255*, 423–429, 1992.

Coakley, J. A., Jr. and R. D. Cess, Response of the NCAR community climate model to the radiative forcing by the naturally occurring tropospheric aerosols, *J. Atmos. Sci.*, *42*, 1677–1692, 1985.

Cosnefroy, H., M. Leroy, and X. Briottet, Selection and characterization of Saharan and Arabian desert sites for the calibration of optical satellite sensors, *Remote Sens. Environ.*, *58*, 101–114, 1996.

Deering, D. W., T. F. Eck, and J. Otterman, Bidirectional reflectances of selected desert areas and their 3-parameter soil characterization, *Agric. For. Meteorol.*, *52*, 71–93, 1990.

Deering, D. W., T. F. Eck, and T. Grier, Shinnery oak bidirectional reflectance properties and canopy model inversion, *IEEE Trans. Geosci. Remote Sens.*, *30*, 339–348, 1992.

Deschamps, P. Y., F. M. Bréon, M. Leroy, A. Podaire, A. Bricaud, J. C. Buriez, and G. Sèze, The POLDER mission: Instrument characteristics and scientific objectives, *IEEE Trans. Geosci. Remote Sens.*, *32*, 598–615, 1994.

Dickinson, R. E., Modeling evapotranspiration for three-dimensional

global climate models, in *Climate Processes and Climate Sensitivity*, *Geophys. Monogr. Ser.*, vol. 29, edited by J. E. Hansen and T. Takahashi, pp. 58–72, AGU, Washington, D. C., 1984.

Dulac, F., D. Tanré, G. Bergametti, P. Buat-Ménard, M. Desbois, and D. Sutton, Assessment of the African airborne dust mass over the western Mediterranean Sea using Meteosat data, *J. Geophys. Res.*, *97*, 2489–2506, 1992.

Field, C. B., J. T. Randerson, and C. M. Malmström, Global net primary production: Combining ecology and remote sensing, *Remote Sens. Environ.*, *51*, 74–88, 1995.

Fraser, R. S., Satellite measurement of mass of Saharan dust in the atmosphere, *Appl. Opt.*, *15*, 2471–2479, 1976.

Fraser, R. S., Y. J. Kaufman, and R. L. Mahoney, Satellite measurements of aerosol mass and transport, *Atmos. Environ.*, *18*, 2577–2584, 1984.

Frouin, R., P. Y. Deschamps, and P. Lecomte, Determination from space of total atmospheric water vapor amounts by differential absorption near 940 nm: Theory and airborne verification, *J. Appl. Meteorol.*, *29*, 448–460, 1990.

Fung, I. Y., C. J. Tucker, and K. C. Prentice, Application of advanced very high resolution radiometer vegetation index to study atmosphere-biosphere exchange of CO_2, *J. Geophys. Res.*, *92*(D3), 2999–3015, 1987.

Gao, B. C., and A. F. H. Goetz, Column atmospheric water vapor retrievals from airborne imaging spectrometer data, *J. Geophys. Res.*, *95*, 3549–3564, 1990.

Goel, N. S., Models of vegetation canopy reflectance and their use in estimation of biophysical parameters from reflectance data, *Remote Sens. Rev.*, *4*, 1–212, 1988.

Goloub, P., J. L. Deuzé, M. Herman, and Y. Fouquart, Analysis of the POLDER polarization measurements over cloud covers, *IEEE Trans. Geosci. Remote Sens.*, *32*, 78–88, 1994.

Gutman, G. G., The derivation of vegetation indices from AVHRR data, *Int. J. Remote Sens.*, *8*, 1235–1243, 1987.

Gutman, G. G., Vegetation indices from AVHRR: An update and future prospects, *Remote Sens. Environ.*, *35*, 121–136, 1991.

Hautecoeur, O., and M. Leroy, Intercomparison of several BRDF models for the compositing of POLDER data over land surfaces, in *Proceedings of the IGARSS'96 Conference*, edited by T. I. Stein, pp. 204–208, *Lincoln, Nebraska*, IEEE Publications, Piscataway, N. J., 1996.

Herman, M., J. L. Deuzé, C. Devaux, P. Goloub, F. M. Bréon, and D. Tanré, Remote sensing of aerosols over land surfaces, including polarization measurements: Application to some airborne POLDER measurements, *J. Geophys. Res.*, this issue.

Holben, B. N., T. F. Eck, and R. S. Fraser, Precipitable water in the Sahel measured using Sun photometry, *Agric. For. Meteorol.*, *52*, 95–107, 1990.

Holben, B. N., E. Vermote, Y. J. Kaufman, D. Tanré, and V. Kalb, Aerosols retrieval over land from AVHRR data—Application for atmospheric corrections, *IEEE Trans. Geosci. Remote Sens.*, *30*, 212–222, 1992.

Hoppel, W. A., J. W. Fitzgeral, G. M. Frick, R. E. Larson, and E. J. Mack, Aerosol size distribution and optical properties found in the marine boundary layer over the Atlantic Ocean, *J. Geophys. Res.*, *95*, 3659–3686, 1990.

Huete, A. R., A soil-adjusted vegetation index (SAVI), *Remote Sens. Environ.*, *25*, 295–309, 1988.

Jacquemoud, S., F. Baret, B. Andrieu, F. M. Danson, and K. Jaggard, Extraction of vegetation biophysical parameters by inversion of the PROSPECT+SAIL model on sugar beet canopy reflectance data—Application to TM data, *Remote Sens. Environ.*, *52*, 163–172, 1995.

Jupp, D. L. B., and A. H. Strahler, A hot spot model for leaf canopies, *Remote Sens. Environ.*, *38*, 193–210, 1991.

Justice, C. O., J. R. G. Townshend, B. N. Holben, and C. J. Tucker, Analysis of the phenology of global vegetation using meteorological satellite data, *Int. J. Remote Sens.*, *6*, 1271–1318, 1985.

Justice, C., T. Eck, D. Tanré, and B. N. Holben, The effect of water vapour on the NDVI derived for the Sahelian region from NOAA/AVHRR data, *Int. J. Remote Sens.*, *12*, 1165–1187, 1991.

Kaufman, Y. J., and B. C. Gao, Remote sensing of water vapor in the near IR from EOS/MODIS, *IEEE Trans. Geosci. Remote Sens.*, *30*, 871–884, 1992.

Kaufman, Y. J., and T. Nakajima, Effect of Amazon smoke on cloud microphysics and albedo—Analysis from satellite imagery, *J. Appl. Meteorol.*, *32*, 729–744, 1993.

Kaufman, Y. J., and C. Sendra, Algorithms for atmospheric corrections of visible and near IR satellite imagery, *Int. J. Remote Sens.*, *9*, 1357–1381, 1988.

Kaufman, Y. J., and D. Tanré, Atmospheric Resistant Vegetation Index (ARVI) for EOS-MODIS, *IEEE Trans. Geosci. Remote Sens.*, *30*, 261–270, 1992.

Kaufman, Y. J., and D. Tanré, Strategy for direct and indirect methods for correcting the aerosol effect on remote sensing: From AVHRR to EOS-MODIS, *Remote Sens. Environ.*, *55*, 65–79, 1996.

Kaufman, Y. J., R. S. Fraser, and R. A. Ferrare, Satellite measurements of large-scale air pollution methods, *J. Geophys. Res.*, *95*(D7), 9895–9909, 1990.

King, M. D., Y. J. Kaufman, W. P. Menzel, and D. Tanré, Remote sensing of cloud, aerosol, and water vapor properties from the moderate resolution imaging spectroradiometer, *IEEE Trans. Geosci. Remote Sens.*, *30*, 7–27, 1992.

Kuusk, A., A multispectral canopy reflectance model, *Remote Sens. Environ.*, *50*, 75–82, 1994.

Legrand, M., M. Desbois, and K. Vovor, Satellite detection of Saharan dust: Optimized imaging during nighttime, *J. Clim.*, *1*, 256–264, 1988.

Legrand, M., J. J. Bertrand, M. Desbois, L. Menager, and Y. Fouquart, The potential of infrared satellite data for the retrieval of Saharan dust optical depth over Africa, *J. Appl. Meteorol.*, *28*, 309–318, 1989.

Leroy, M., and F. M. Bréon, Surface reflectance angular signatures from airborne POLDER data, *Remote Sens. Environ.*, *57*, 97–107, 1996.

Leroy, M., and J. L. Roujean, Sun and view angle corrections on reflectances derived from NOAA/AVHRR data, *IEEE Trans. Geosci. Remote Sens.*, *32*, 684–696, 1994.

Li, X., A. H. Strahler, and C. E. Woodcock, A hybrid geometric optical-radiative transfer approach for modeling albedo and directional reflectance of the discrete crown vegetation canopy, *IEEE Trans. Geosci. Remote Sens.*, *33*, 466–480, 1995.

Liang, S., and A. H. Strahler, Retrieval of surface BRDF from multiangle remotely sensed data, *Remote Sens. Environ.*, *50*, 18–30, 1994.

Maisongrande, P., A. Ruimy, G. Dedieu, and B. Saugier, Monitoring seasonal and interannual variations of gross primary productivity, net primary productivity, and net ecosystem productivity using a diagnostic model and remotely sensed data, *Tellus*, *47B*, 178–190, 1995.

Matthews, E., Global vegetation and land use: New high resolution data bases for climate studies, *J. Clim. Appl. Meteorol.*, *22*, 474–487, 1983.

Nilson, T., and A. Kuusk, A reflectance model for the homogeneous plant canopy and its inversion, *Remote Sens. Environ.*, *27*, 157–167, 1989.

Parol, F., P. Goloub, M. Herman, and J. C. Buriez, Cloud altimetry and water phase retieval from POLDER instrument during EUCREX'94, *The European Symposium on Satellite Remote Sensing*, Atmospheric Sensing and Modeling, *Proc. SPIE Int. Soc. Opt. Eng.*, *2311*, 171–181, 1994.

Pinty, B., M. M. Verstraete, and R. E. Dickinson, A physical model of the bidirectional reflectance of vegetation canopies, 2, Inversion and validation, *J. Geophys. Res.*, *95*, 11,767–11,775, 1990.

Prince, S. D., A model of regional primary production for use with coarse-resolution satellite data, *Int. J. Remote Sens.*, *12*, 1313–1330, 1991.

Rahman, H., B. Pinty, and M. M. Verstraete, A coupled surface-atmosphere reflectance (CSAR) model, 2, A semiempirical surface model useable with NOAA/AVHRR data, *J. Geophys. Res.*, *98*, 20,791–20,801, 1993.

Rind, D., E.-W. Chiou, W. Chu, J. Larsen, S. Oltmans, J. Lerner, M. P. McCormick, and L. MacMaster, Positive water vapor feedback in climate models confirmed by satellite data, *Nature*, *349*, 500–503, 1991.

Rondeaux, G., and M. Herman, Polarization of light reflected by crop canopies, *Remote Sens. Environ.*, *38*, 63, 1991.

Roujean, J. L., and F. M. Bréon, Estimating PAR absorbed by vegetation from bidirectional reflectance measurements, *Remote Sens. Environ.*, *51*, 375–384, 1995.

Roujean, J. L., M. Leroy, A. Podaire, and P. Y. Deschamps, Evidence of surface bidirectional effects from a NOAA/AVHRR multitemporal data set, *Int. J. Remote Sens.*, *13*(4), 685–698, 1992a.

Roujean, J. L., M. Leroy, and P. Y. Deschamps, A bidirectional re-

flectance model of the Earth's surface for the correction of remote sensing data, *J. Geophys. Res.*, *97*(D18), 20,455–20,468, 1992b.

Ruimy, A., G. Dedieu, and B. Saugier, Methodology for the estimation of terrestrial net primary production from remotely sensed data, *J. Geophys. Res.*, *99*(D3), 5263–5283, 1994.

Running, S. W., et al., Terrestrial remote sensing science and algorithms planned for EOS/MODIS, *Int. J. Remote Sens.*, *15*, 3587–3620, 1994.

Scott, N. A., A direct method of computation of the transmission function of an inhomogeneous gaseous medium, I, Description of the method, *J. Quant. Spectrosc. Radiat. Transfer*, *14*, 691–704, 1974.

Sellers, P. J., C. J. Tucker, G. J. Collatz, S. O. Los, C. O. Justice, D. A. Dazlich, and D. A. Randall, A global 1° by 1° NDVI data set for climate studies, 2, The generation of global fields of terrestrial biophysical parameters from the NDVI, *Int. J. Remote Sens.*, *15*, 3519–3545, 1994.

Shibayama, M., and C. L. Wiegand, View azimuth and zenith, and solar angle effects on wheat canopy reflectance, *Remote Sens. Environ.*, *18*, 91–103, 1985.

Swap, R., M. Garstang, S. Greco, R. Talbot, and P. Kallberg, Saharan dust in the Amazon basin, *Tellus*, *44B*, 133–149, 1992.

Tanré, D., P. Y. Deschamps, C. Devaux, and M. Herman, Estimation of Saharan aerosol optical thickness from blurring effect in Thematic Mapper data, *J. Geophys. Res.*, *93*, 15,955–15,964, 1988.

Tanré, D., C. Deroo, P. Duhaut, M. Herman, J. Morcrette, J. Perbos, and P. Y. Deschamps, Description of a computer code to simulate the satellite signal in the solar spectrum: The 5S code, *Int. J. Remote Sens.*, *11*, 659–668, 1990.

Tanré, D., B. N. Holben, and Y. J. Kaufman, Atmospheric correction algorithm for NOAA-AVHRR products: Theory and application, *IEEE Trans. Geosci. Remote Sens.*, *30*, 231, 1992.

Tarpley, J. P, S. R. Schneider, and R. L. Money, Global vegetation indices from NOAA 7 meteorological satellite, *J. Clim. Appl. Meteorol.*, *23*, 491–494, 1984.

Townshend, J. R. G., C. O. Justice, and V. T. Kalb, Characterization and classification of South American land cover types using satellite data, *Int. J. Remote Sens.*, *8*, 1189–1207, 1987.

Tucker, C. J., J. R. G. Townshend, and T. E. Goff, African land cover classification using satellite data, *Science*, *227*, 369–375, 1985.

Twomey, S. A., M. Piepgrass, and T. L. Wolfe, An assessment of the impact of pollution on the global albedo, *Tellus*, *36B*, 356–366, 1984.

Verhoef, W., Light scattering by leaf layers with application to canopy reflectance modelling: The SAIL model, *Remote Sens. Environ.*, *16*, 125–141, 1984.

Vermote, E., D. Tanré, J. L. Deuzé, and J. J. Morcrette, Second simulation of the satellite signal in the solar spectrum: An overview, *IEEE Trans. Geosci. Remote Sensing*, in press, 1996.

Verstraete, M. M., B. Pinty, and R. E. Dickinson, A physical model of the bidirectional reflectance of vegetation canopies, 1, Theory, *J. Geophys. Res.*, *95*, 11,755–11,765, 1990.

Viovy, N., O. Arino, and A. S. Belward, The best index slope extraction (BISE): A method for reducing noise in NDVI time series, *Int. J. Remote Sens.*, *13*(8), 1585–1590, 1992.

Walthall, C. L., J. M. Norman, J. M. Welles, G. Campbell, and B. L. Blad, Simple equation to approximate the bidirectional reflectance from vegetative canopies and bare soil surfaces, *Appl. Opt.*, *24*(3), 383–387, 1985.

Wu, A., Z. Li, and J. Cihlar, Effects of land cover type and greenness on advanced very high resolution radiometer bidirectional reflectances: Analysis and removal, *J. Geophys. Res.*, *100*(D5), 9179–9192, 1995.

S. Bouffiès, F. M. Bréon, and P. Chazette, LMCE, Commissariat à l'Energie Atomique/Saclay, Bat. 709, L'Orme des Merisiers, 91191 Gif-sur-Yvette Cedex, France.

J. C. Buriez, J. L. Deuzé, M. Herman, and D. Tanré, LOA, USTL-CNRS, 59655 Villeneuve d'Ascq Cedex, France.

O. Hautecoeur and M. Leroy, CESBIO, 18 Avenue E. Belin, 31055 Toulouse Cedex, France.

J. L. Roujean, CNRM, Météo-France, 42 Avenue Gustave Coriolis, 31057 Toulouse Cedex, France.

(Received January 22, 1996; revised July 25, 1996;
accepted August 14, 1996.)